PLASMONICS

Imaging the dark emission of spasers

Hua-Zhou Chen,[1]* Jia-Qi Hu,[1]* Suo Wang,[1]* Bo Li,[1] Xing-Yuan Wang,[1] Yi-Lun Wang,[1] Lun Dai,[1,2] Ren-Min Ma[1,2]†

Spasers are a new class of laser devices with cavity sizes free from optical diffraction limit. They are an emergent tool for various applications, including biochemical sensing, superresolution imaging, and on-chip optical communication. According to its original definition, a spaser is a coherent surface plasmon amplifier that does not necessarily generate a radiative photon output. However, to date, spasers have only been studied with scattered photons, and their intrinsic surface plasmon emission is a "dark" emission that is yet to be revealed because of its evanescent nature. We directly image the surface plasmon emission of spasers in spatial, momentum, and frequency spaces simultaneously. We demonstrate a nanowire spaser with a coupling efficiency to plasmonic modes of 74%. This coupling efficiency can approach 100% in theory when the diameter of the nanowire becomes smaller than 50 nm. Our results provide clear evidence of the surface plasmon amplifier nature of spasers and will pave the way for their various applications.

INTRODUCTION

Lasers are the brightest source of high-frequency electromagnetic radiation. Soon after lasers were invented in 1960 (*1*), they became a key driver of the physical sciences and numerous technologies. The recent rapidly advancing nanoscience and technology call for a nanoscale laser spot for various technologies, such as nanolithography (*2*–*4*), high-density data storage (*5*, *6*), and superresolution imaging (*7*–*9*). However, conventional lasers amplify photons, wherein diffraction limit puts a barrier to scaling down its physical size and mode volume. In 2003, Bergman and Stockman (*10*) proposed a new class of amplifier, named spaser, an acronym for surface plasmon amplification by stimulated emission of radiation. In contrast to the classical laser, a spaser amplifies surface plasmons instead of photons, providing an optical amplifier with a size that is beyond the diffraction limit, which is of major interest in many applications, including biochemical sensing, superresolution imaging, and on-chip optical communication (*11*–*19*). Because of this, numerous studies on the experimental implementation of spasers have been reported (*20*–*32*). However, to date, spasers have only been characterized by the photons scattered to the optical far field (*20*–*32*). According to its original definition, a spaser is a surface plasmon amplifier that does not necessarily generate radiative photon output (*10*, *33*). Its intrinsic surface plasmon emission is a "dark" emission that is yet to be revealed because of its evanescent nature. Consequently, there is a lack of direct evidence of spasing, and the intentional manipulation and use of spaser emission become difficult to achieve.

Here, we directly image surface plasmon emission (an intrinsic but unrevealed feature) of spasers in spatial, momentum, and frequency spaces simultaneously. We demonstrate that spasers can serve as a pure surface plasmon generator with a coupling efficiency to plasmonic modes approaching 100% in theory and experimentally demonstrate a nanowire spaser with a coupling efficiency of 74%. Our results provide clear evidence of spasing behavior, an intrinsic but unrevealed feature of this intensively studied new class of optical amplifiers. Furthermore, in contrast to the scattered photons, the surface plasmon emission of spasers is a crucial element for various nanophotonic applications. The direct imaging and high generation efficiency of these dark emissions will pave the way for various applications of spasers in on-chip nanophotonic circuits (*11*–*14*), nonlinear nanophotonics (*34*–*37*), sensing (*15*–*19*), and imaging (*7*–*9*).

[1]State Key Laboratory for Artificial Microstructures and Mesoscopic Physics, Peking University, Beijing 100871, China. [2]Collaborative Innovation Center of Quantum Matter, Beijing, China.
*These authors contributed equally to this work.
†Corresponding author. Email: renminma@pku.edu.cn

RESULTS AND DISCUSSION

Device fabrication and optical setup

Figure 1A shows a simulated electric field distribution of a spaser that consists of a CdSe nanostrip placed on an Ag film with a thin SiO_2 gap layer in between (section S1). There is a significant amount of energy emitted into the propagating surface plasmon mode supported by the air/Ag interface outside the cavity. These surface plasmon emissions cannot be directly observed at far field because of their evanescent nature. To overcome this limitation, we use leakage radiation microscopy to observe and analyze the emission properties of spasers, as shown in Fig. 1B (see Materials and Methods) (*38*–*40*). For device fabrication, the CdSe nanostrip is synthesized via chemical vapor deposition (CVD) and dry-transferred to a SiO_2/Ag substrate, which is deposited through electron beam evaporation on a borosilicate glass substrate with a thickness of about 0.15 mm (see Materials and Methods). The thicknesses of Ag and SiO_2 films are 50 and 5 nm, respectively. The thicknesses of the glass substrate and the Ag film are optimized for leakage radiation microscopy. For optical characterization, the device is optically pumped from the top, and the emission is collected by an oil immersion objective underneath with a large numerical aperture (NA) of 1.40 (sections S2 and S3).

Imaging the dark emission of a single-mode spaser

To provide direct evidence for lasing in spasers, we first image the emission of a single-mode spaser in spatial, momentum, and frequency spaces. The single-mode operation was achieved in an irregularly shaped device where only a limited number of modes can compete for gain because of its lower symmetry (*23*). The inset of Fig. 2A shows the scanning electron microscope (SEM) image of the single-mode spaser with dimensions of about 4.06 μm (length) × 2 μm (width) × 70 nm (thickness). Note that its thickness is only $^1/_{10}$ of the emission wavelength (~700 nm). Because of the deep subwavelength thickness, the CdSe nanostrip spaser–supported transverse magnetic (TM) mode (with the dominant magnetic field component parallel to the metal surface) strongly hybridizes with the plasmonic mode, resulting in strong field confinement within the metal-insulator-semiconductor interface (*22*, *23*). This hybridization leads to a marked increase in the effective

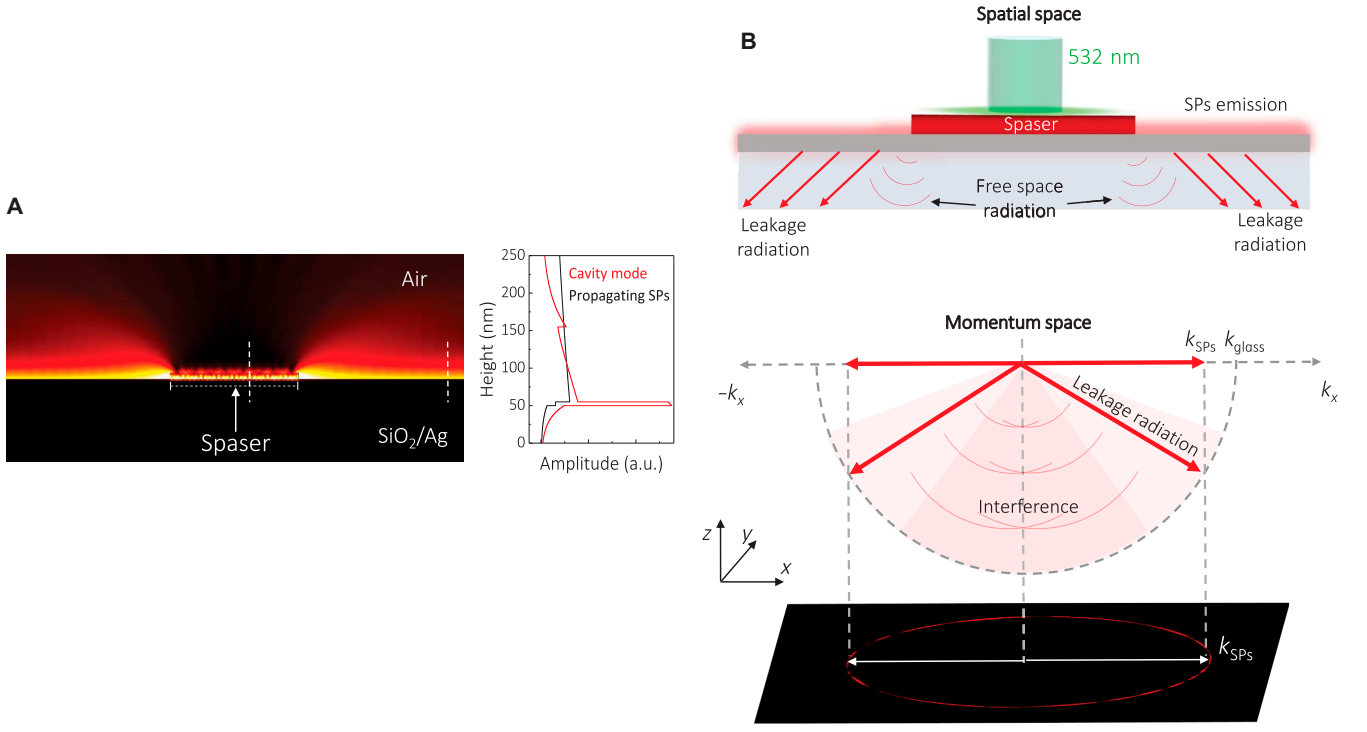

Fig. 1. Imaging the dark emission of spasers by leakage radiation microscopy. (**A**) Left: Electric field distribution of a spaser in a two-dimensional simulation, where we can see that most emission of the spaser couples to propagating surface plasmons. Right: The surface plasmon mode profiles in and out of the spaser cavity. (**B**) Schematic of leakage radiation microscopy for imaging emission of spasers in spatial (top) and momentum (bottom) spaces.

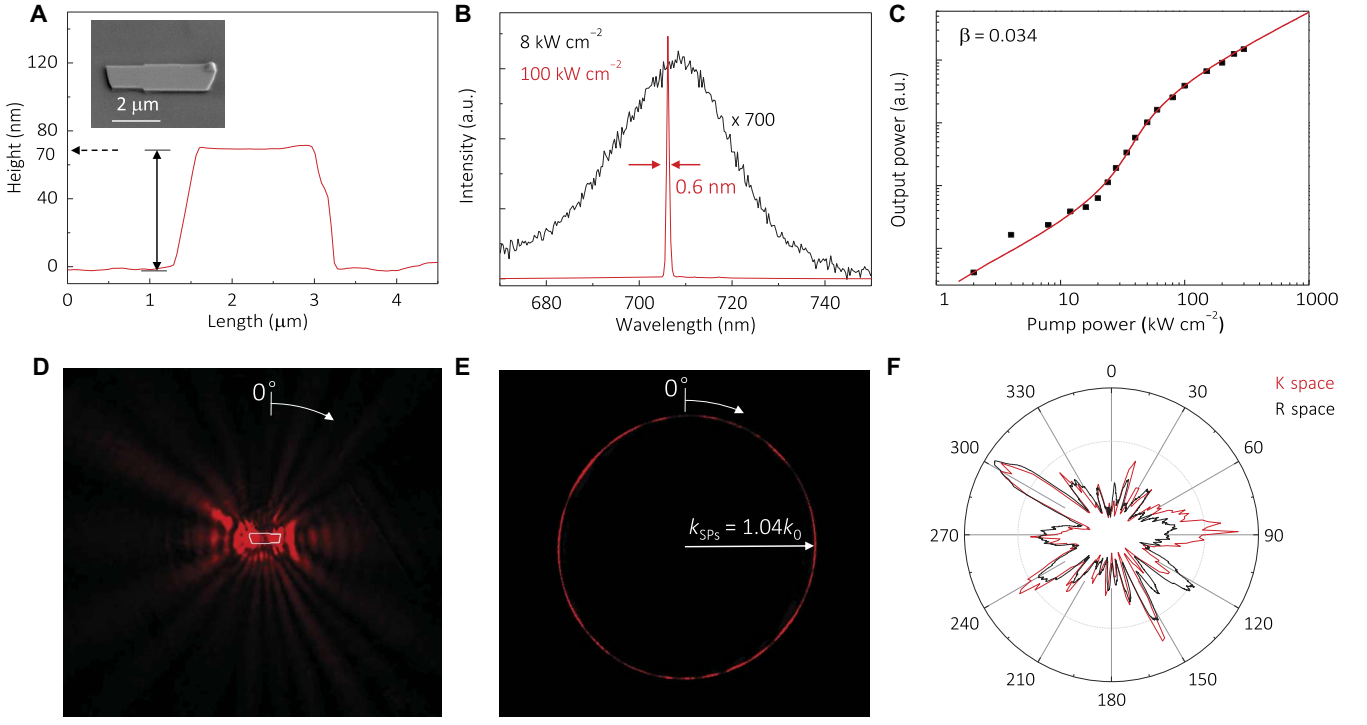

Fig. 2. Simultaneously obtained emission images of a spaser in spatial, frequency, and momentum spaces. (**A**) SEM image (inset) and the atomic force microscopy–measured profile of the spaser device. The length, width, and thickness are about 4.06 μm, 2 μm, and 70 nm, respectively. (**B**) Emission spectrum of the spaser shows that the device experiences a transition from spontaneous emission to full laser oscillation with an increase in pump power. (**C**) Integrated light output versus pump response. (**D** and **E**) Spatial space (D) and momentum space (E) images of the spaser emission obtained via leakage radiation microscopy (false color). (**F**) Azimuthal distribution of the spaser emission obtained from spatial space (black) and momentum space (red) images.

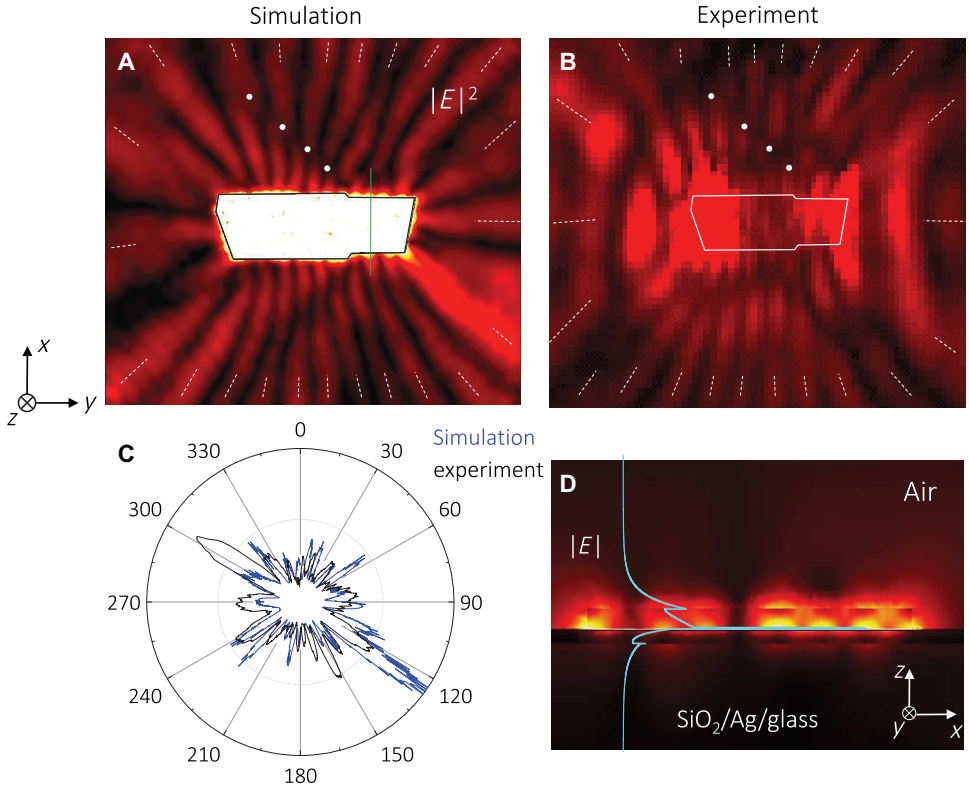

Fig. 3. Lasing plasmonic mode of a spaser. (**A** and **B**) Three-dimensional full wave simulated surface plasmon mode (A) supported by the plasmon cavity depicted in Fig. 2 that matched the experimental one (B) (false color). (**C**) Azimuthal distribution of the spaser emission obtained from spatial space images (black) and the full wave simulation (blue). (**D**) Electric distribution of the simulated mode on the *zy* plane in log scale, which exhibits the signature of a plasmonic mode.

refractive index, which increases the reflection coefficient at the CdSe nanostrip boundaries, resulting in a strong cavity feedback (*23*). On the other hand, the transverse electric (TE) mode (with the dominant electric field component parallel to the metal surface) cannot hybridize with the plasmonic mode. Consequently, it becomes delocalized with respect to the TE mode of the CdSe alone. Although both TM and TE modes are free to propagate in the plane, the TM mode has a much larger effective refractive index and thus a significantly lower radiation loss to achieve the necessary feedback for lasing (*23*).

To achieve lasing state, we pumped the spaser with a 532-nm nanosecond laser. With an increase in pump power, the device experiences a transition from spontaneous emission to full single-mode spaser oscillation. The lasing behavior is evidenced by both the rapid increase in spectral purity, wherein the lasing peak is more than two orders of magnitude higher than the spontaneous emission background (Fig. 2B), and the clear threshold behavior in integrated light output versus pump response (Fig. 2C). The full width at half maximum of the lasing peak is about 0.6 nm. The lasing threshold readout from the light-light curve in Fig. 2C is 35 kW cm^{-2}.

The emission of the spaser partially scatters to free space and partially couples to the plasmonic mode supported by the air/Ag interface outside the cavity. The lasing emission collected by the oil immersion lens contains the information of both parts. The scattered photon emission penetrates the silver substrate with attenuation, whereas the emission coupled to the plasmonic mode leaks into the substrate at a certain polar angle that satisfies the momentum match condition (see Materials and Methods) (*38*–*40*).

Figure 2 (D and E) shows images of the spaser emission in the spatial and momentum spaces obtained with leakage radiation microscopy. In the spatial space image (Fig. 2D), there are discrete emission beams from the spaser. In the momentum space image, we can see that most of the emission is located on a ring with a radius of $1.04k_0$ (section S4), where k_0 is the free-space wave number of the emitted 700-nm wave. This thin ring-shaped momentum space image is a signature of the leakage surface plasmon radiation (*38*–*40*). The directions of discrete emission beams in the spatial space image match the azimuthal brightness fluctuation in the momentum space image well (Fig. 2F), indicating that these are dominantly surface plasmon emissions of the spaser propagating in the air/Ag interface.

The pronounced anisotropic azimuthal distribution of the emission does not change with pump power and is the fingerprint of a cavity eigenmode, which helped us to identify the exact lasing mode (section S5). Using a three-dimensional full wave simulation, we found a cavity eigenmode that matches the lasing mode observed in the experiment well, as shown in Fig. 3 (A to C). We can see that both the simulated and experimental patterns have 23 distinguishable emission beams, marked by white dashed lines, and most of these emission beams match each other in emission directions. Furthermore, on the top middle of the patterns, dislocations of a few emission beams match each other in the simulated pattern and in the experimental one. We also observe interference patterns in both spatial space and momentum space images, which match the simulated results (sections S6 and S7). Although the simulated and experimental patterns share good similarity, they are not perfectly matched because we are not able to perfectly

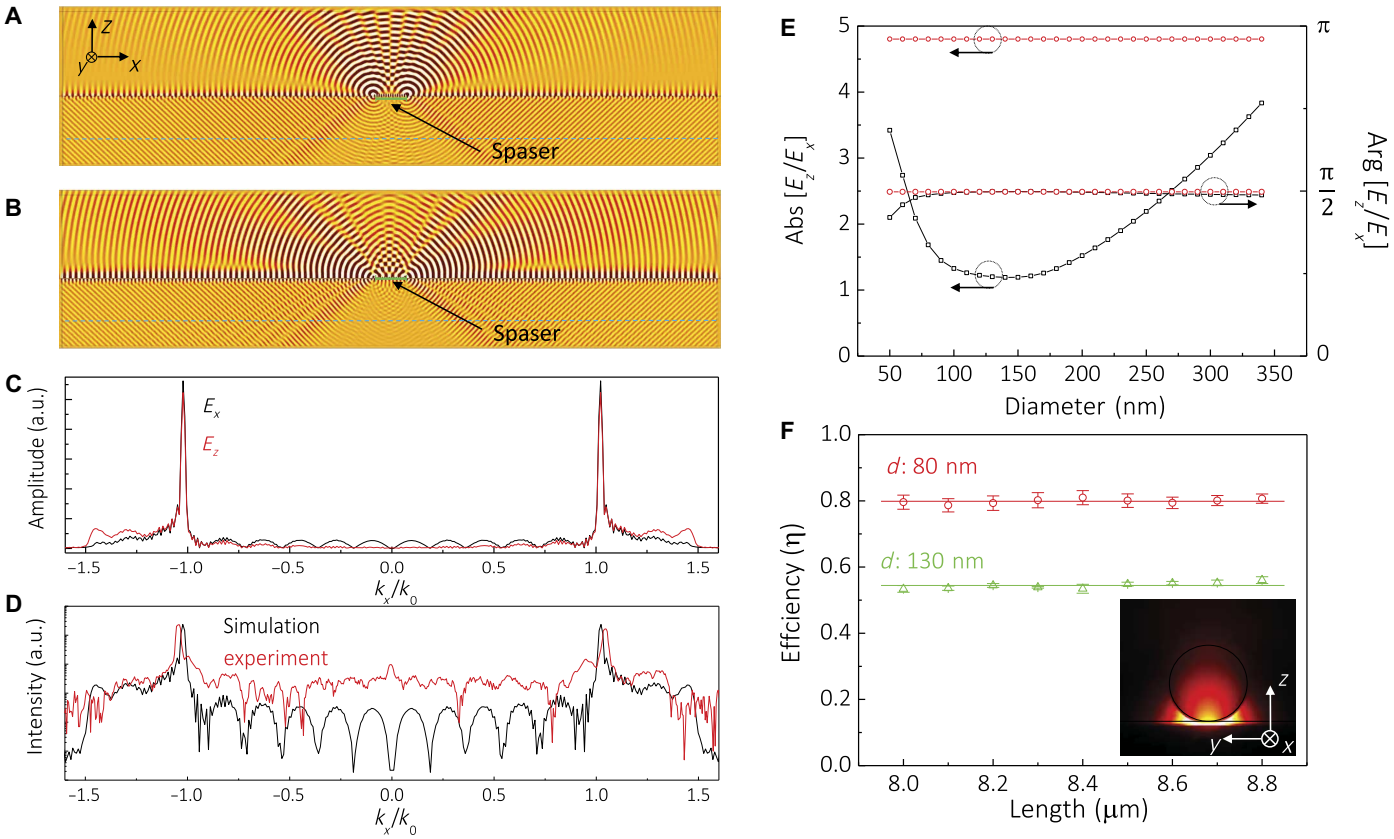

Fig. 4. Determinants of surface plasmon generation efficiency. (**A** and **B**) The full wave simulated E_x (A) and E_z (B) field distribution of a spaser cavity with a length of 4.06 μm. (**C**) The fast Fourier–transformed E_x and E_z fields of the leakage surface plasmons 5 μm below the Ag film, indicated by the green broken lines in (A) and (B). (**D**) The fast Fourier–transformed total electric field (black) and experimental result obtained from the momentum space image of the spaser depicted in Fig. 2 (red). (**E**) Amplitude and phase of E_z/E_x of the fundamental plasmonic cavity mode at various nanowire diameters (black curves) and the surface plasmon mode supported by the air/Ag interface outside the cavity (red curves). (**F**) Surface plasmon generation efficiency (η) of nanowire cavities with different lengths, which have diameters of 80 and 130 nm. η is calculated by averaging the different orders of longitudinal modes of fundamental plasmonic modes around a wavelength of 700 nm. Error bar represents the SD of η of the different longitudinal modes. Inset: The simulated electric field distribution of the fundamental plasmonic mode.

rebuild such a large and irregular cavity in the simulation. The matched mode is a plasmonic mode, with the field strongly confined in the metal-insulator-semiconductor interface (Fig. 3D). The mode volume is about 0.017 μm^3, and the cavity quality factor is about 22, limited by metal loss (see Materials and Methods). In a spaser, the excited electron-hole pairs in the gain medium recombine and then radiate directly into surface plasmons because of their high emission rate, which is accelerated by the Purcell factor (*22*, *23*). This excitation-relaxation process of surface plasmon generation does not need the external laser and sophisticated setup required for the indirect generation of surface plasmons by phase match, which is an intrinsic property of spasers as a surface plasmon amplifier, according to its original definition (*10*, *33*).

Surface plasmon generation efficiency calculation

We have revealed the essential emission properties of a spaser. The precisely determined single-mode lasing emission in spatial, frequency, and momentum spaces provides clear evidence for lasing in plasmonic mode. We can then extract the full properties of the plasmonic lasing mode from the confirmed eigenmode in three-dimensional full wave simulations. Next, we study the surface plasmon generation efficiency (η) of spasers. Here, η is defined as P_{SPs}/P_{total}, where P_{SPs} and P_{total} are the surface plasmon emission power and the total emission power of a spaser, respectively. The surface plasmon emission is a TM wave with magnetism polarization parallel to the silver surface. We calculate the P_{SPs} by integrating its corresponding Poynting vector on four surfaces perpendicular to the silver plane surrounding the spaser cavity and the P_{total} by integrating the total power outflow over a surface enclosing the device (section S8).

We first study the determinants of η. To get an understanding of the spaser cavity–propagating plasmonic mode coupling, we simulate the electric field distribution of a spaser device with a cavity length of 4.06 μm, similar to the device shown in Fig. 2 but with an infinite width. Figure 4 (A and B) shows the simulated E_x field (electric field parallel to the metal surface) and E_z field (electric field perpendicular to the metal surface) distributions of the spaser cavity, respectively. Note that the E_y field is negligible compared to the E_x field and E_z field. As shown in Fig. 4 (A and B), the E_x field is dominantly scattered in the free space where the two ends of the spaser cavity act as two point sources, whereas the E_z field is dominantly coupled to the surface plasmon mode supported by the air/Ag interface. The obtained E_x and E_z fields of the leakage plasmons (5 μm below the Ag film) are Fourier-transformed to momentum space image (Fig. 4C). We can see that the strongest field is located on a ring with a wave number of $1.022k_0$, indicating that the main radiation is from leakage surface plasmons. We calculate the intensity of the total electric field by summing up the simulated E_x^2

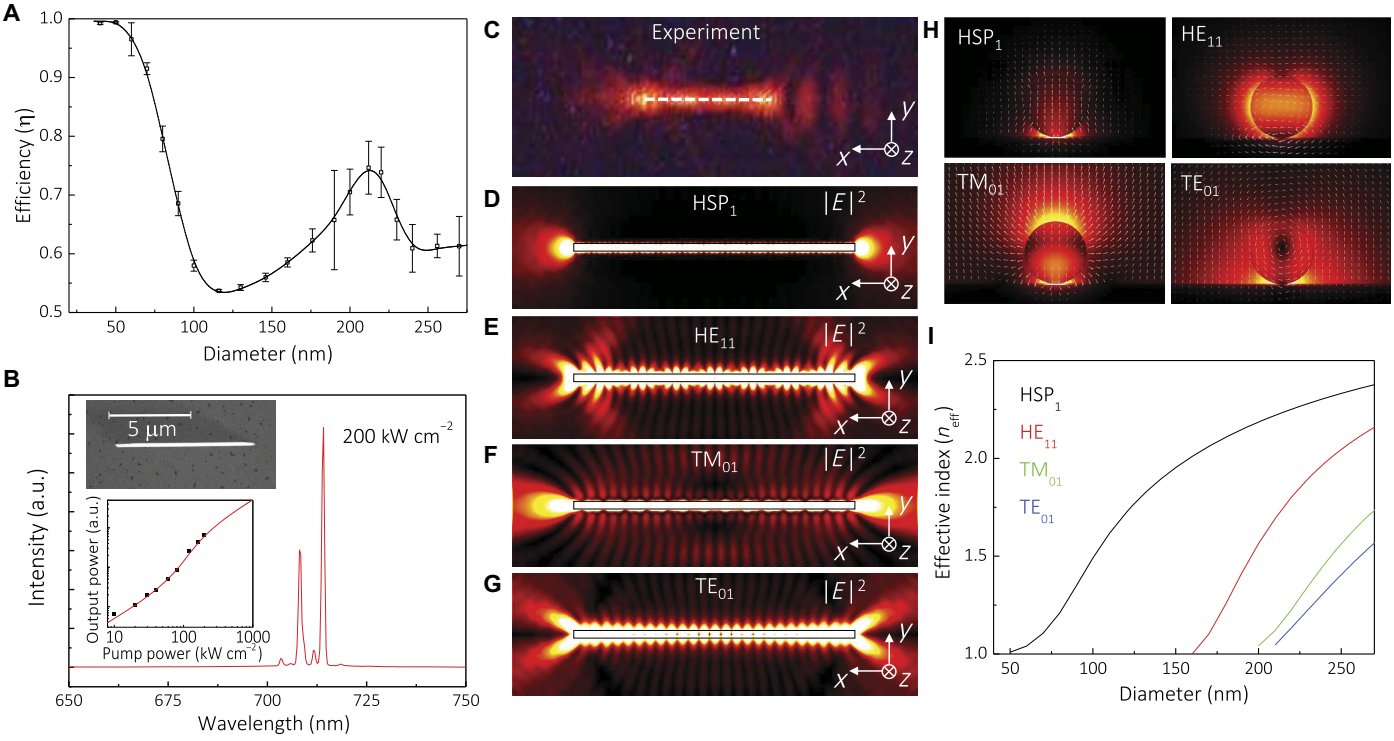

Fig. 5. Nanowire spasers with high surface plasmon generation efficiency. (**A**) Surface plasmon generation efficiencies of nanowire spasers with varied diameters operated at the fundamental plasmonic mode. The length of the cavity is 8.4 μm. (**B**) Spectrum, SEM image, and light-light curve of a nanowire spaser with a length of 8.4 μm and a diameter of 212 nm. (**C**) Spatial space image of the nanowire spaser emission depicted in (B). (**D** to **G**) Electric field distribution of four transverse modes supported by the 212-nm-diameter and 8.4-μm-long cavity in three-dimensional simulation. The fundamental plasmonic mode has a similar emission pattern to the experimental one, whereas the other three modes differ in their pronounced emission perpendicular to the nanowire long axis. (**H**) Simulated electric field distribution (*yz* plane) of the four modes depicted in (D) to (G); the white arrow shows their polarization distribution. (**I**) Effective refractive index with various diameters in two-dimensional simulation of the four modes depicted in (D) to (G).

and E_z^2. The key features, including the peak position of the leakage surface plasmon radiation and the interference pattern of the scattered photons, match the experimental results well, as shown in Fig. 4D. The preferentially scattering polarization observed here is due to the plasmonic cavity mode containing more E_x field than the plasmonic mode supported by the air/Ag interface outside the cavity (section S9).

Nanowire spasers with high surface plasmon generation efficiency

Next, we focus on nanowire spasers and their fundamental transverse plasmonic modes. The nanowire configuration simplifies derivation because of its highly symmetric cross section. The fundamental mode has the strongest field confinement and cavity feedback for lasing. Figure 4E shows the calculated amplitude and phase of E_z/E_x of the fundamental plasmonic cavity mode at various nanowire diameters. For a comparison, we also plot the E_z/E_x of the plasmonic mode supported by the air/Ag interface outside the cavity in the figure. The amplitude of E_z/E_x of the cavity mode first decreases with the increase of the nanowire diameter and then starts to increase when a diameter of around 130 nm is reached (section S9). The phase of the ratio is about π/2 and not sensitive to the nanowire diameter. A larger E_z/E_x means weaker E_x scattering and, thus, larger η. Note that the E_z/E_x mainly depends on the effective refractive index of the cavity mode and is thus not sensitive to the length of the cavity and the order of the longitudinal mode, and so should be the η. In three-dimensional full wave simulations, we calculate the η of nanowire cavities with different lengths, which have diameters of 80 and 130 nm. We average the efficiency of different orders of longitudinal modes of the fundamental transverse plasmonic mode around the wavelength of 700 nm for each cavity configuration. As shown in Fig. 4F, the η is invariant for different lengths and longitudinal modes, as expected.

We then calculate the η of nanowire spasers with various diameters using three-dimensional full wave simulations. As shown in Fig. 5A, the η of the fundamental mode approaches 100% when the diameter of the nanowire becomes smaller than 50 nm. In this range, spasers become a pure surface plasmon generator and do not radiate photon output.

In a large range, η is higher than 53%. We can see that the main tendency of η with a diameter is consistent with that of E_z/E_x. Modulation occurs at a diameter larger than about 200 nm because the fundamental plasmonic mode shifts from a more surface plasmon–like mode to a more photonic-like mode (section S10). The η reaches 74% at a diameter of about 210 nm. Considering that a device with a larger diameter has a higher effective index and a larger confinement factor for low-threshold lasing, we optimize the diameter of the nanowire to be about 210 nm for the demonstration of a spaser with high η.

Figure 5B shows the SEM image, lasing spectrum, and light-light curve of a spaser with a diameter of about 212 nm and a length of 8.4 μm. The lasing threshold is about 70 kW cm^{-2}. Above the threshold, the device exhibits multiple laser peaks attributed to the multilongitudinal modes in the nanowire cavity configuration. Figure 5C shows the spatial space image. It can be seen that the emission mainly directs along the nanowire long axis. For the cavity with a diameter of 212 nm,

we have confirmed that there are four transverse modes using two- and three-dimensional simulations (section S11). Figure 5 (D to G) shows the electric field distributions of these four eigenmodes supported by the 212-nm-diameter and 8.4-μm-long cavity in three-dimensional simulation. One can see that the fundamental plasmonic mode has a similar emission pattern to the experimental one, whereas the other three modes differ in their pronounced emission perpendicular to the nanowire long axis. The lasing in the fundamental plasmonic mode at this cavity diameter is due to its best field confinement and largest effective index for cavity feedback, as shown in Fig. 5 (H and I), to compete for gain over other cavity modes. From the three-dimensional full wave simulation, the η of this laser device was determined to be about 74%. Note that we also study the momentum space images of nanowire spasers, which are similar to the one shown in Fig. 2 (section S12).

CONCLUSION

In conclusion, we directly image surface plasmon emission of spasers in spatial, momentum, and frequency spaces simultaneously, providing clear evidence for plasmonic lasing. We demonstrate that spasers can serve as a pure surface plasmon generator with an efficiency approaching 100% in theory and experimentally demonstrate a nanowire spaser with a coupling efficiency of 74%. The advantages of spasers serving as coherent surface plasmon generators are threefold: (i) the generation of surface plasmons relies on a carrier excitation-relaxation process, which does not need the phase match requirement in other methods; (ii) the cavity modes of spasers can share a similar profile with the propagating surface plasmon modes outside of the cavity, which will ensure high coupling efficiency; (iii) spasers are equipped with a small footprint suitable for large-scale on-chip integration. The precisely determined emission of spasers in spatial, frequency, and momentum spaces and the high surface plasmon generation efficiency pave the way for intentional spaser emission manipulation and its various applications in on-chip nanophotonic circuits, nonlinear nanophotonics, sensing, and imaging.

MATERIALS AND METHODS

Device fabrication

CdSe nanostrips were synthesized via the CVD method (*41*). CdSe (99.999%) powder was used as the source and placed on a quartz boat inside the tube furnace. Pieces of Si (100) wafers covered with 10-nm-thick Au catalyst films were used as substrates, which were loaded on the quartz boat 15 to 17 cm downstream of the CdSe powder. The tube was kept in vacuum under a constant high-purity argon flow at a rate of 20 standard cubic centimeters per minute. The growth temperature and duration were about 710°C and 1 hour, respectively. After the synthesis, CdSe nanostrips were dry-transferred to SiO_2/Ag (5 nm/50 nm) substrates that were deposited through electron beam evaporation on a borosilicate glass substrate of no. 1 thickness (~0.15 mm) for the construction of spasers.

Leakage radiation microscopy setup

The microscope was built against an oil immersion objective with a large NA of 1.40, which comprises two major parts: (i) the top excitation part and (ii) the bottom collection part. For the top excitation part, a Q-switched nanosecond semiconductor laser was used to pump the nanostrips from the top of the device (λ_{pump} = 532 nm; repetition rate, 1 to 2 kHz; pulse length, 4.5 ns). A lens with a focal length of 100 mm focuses the pump beam to an approximately 10-μm-diameter spot on the sample. The power of the pump light was controlled by a variable attenuator and measured by a power meter. For the bottom collection part, the signal was collected with an oil immersion objective with a large NA of 1.40 underneath the device and guided to charge-coupled devices and spectrometers for imaging in spatial, momentum, and frequency spaces. All experiments were carried out at room temperature.

Momentum matching condition for leakage radiation

The collected lasing emission by the oil immersion lens contained the information of both leakage surface plasmon and scattered photon emission. While the scattered photon emission penetrated the silver substrate with attenuation, the emission coupled to the surface plasmon mode leaked into the substrate at a certain polar angle that satisfied the momentum matching condition. The momentum matching condition required the wave vector of the surface plasmon mode propagating in the air/Ag interface (k_{SPP}) to be equal to the component of the wave vector parallel to the plane wave substrate in a glass substrate ($k_{glass\|}$) (*38*).

Numerical mode simulations

Optical modes of the spasers were calculated via the finite-element method (COMSOL Multiphysics). In this model, the CdSe nanostrip (ε_{CdSe} = 7.84) lay in contact with a 5-nm SiO_2 (ε_{SiO_2} = 2.16) gap layer above a Ag substrate (ε_{Ag} = − 23.062 − 2.36286*i*). The permittivity of the glass substrate was set to be 2.289. The effective mode volume of the lasing plasmon cavity was calculated as

$$V_{eff} = \frac{\int W_{em}(\vec{r})\, d^3\vec{r}}{\varepsilon_0 \varepsilon(|\vec{E}|^2_{max})}$$

where W_{em} is the electromagnetic energy density of the mode and $\vec{E}$ is the evaluated maximal electric field. Taking into account the strongly dispersive property of silver, $W_{em}(\vec{r})$ is equal to

$$\frac{1}{2}\left[Re\left[\frac{d(\omega\varepsilon)}{d\omega}\right]|\vec{E}(\vec{r})|^2 + \mu|\vec{H}(\vec{r})|^2\right]$$

where the dispersive parameter was obtained from fitting the experimental results. The *Q* factors of the cavity modes were calculated from the formula $Q = f_r/\Delta f$, where f_r is the resonance frequency and Δf is the full width at half maximum of the resonance spectrum.

SUPPLEMENTARY MATERIALS

Supplementary material for this article is available at http://advances.sciencemag.org/cgi/content/full/3/4/e1601962/DC1

section S1. Schematic of spasers
section S2. Imaging principle
section S3. Optical setup
section S4. Calibration in momentum space
section S5. Lasing spectra and emission patterns at varied pump powers
section S6. Interference in the momentum space image
section S7. Interference in the spatial space image
section S8. Surface plasmon generation efficiency
section S9. Preferentially scattering polarization
section S10. Peak value of η at a diameter of around 210 nm
section S11. Transverse modes supported by nanowire spaser cavity

section S12. Momentum space image of a nanowire spaser
fig. S1. Schematics of spaser configurations studied in this work.
fig. S2. Schematics of imaging principles.
fig. S3. Schematic of leakage radiation microscopy setup.
fig. S4. Calibration in the momentum spaces.
fig. S5. Spectrum and spatial emission patterns of the spaser shown in Fig. 2 under different pump powers.
fig. S6. Interference of scattered photon emission in the momentum spaces.
fig. S7. Interference in the spatial space image.
fig. S8. Calculation of surface plasmon generation efficiency.
fig. S9. Effective index for the calculation of the E_z/E_x ratio of a surface plasmon cavity mode.
fig. S10. The proportion of surface plasmon mode in HSP_1 mode versus nanowire diameter.
fig. S11. Four transverse modes supported by a nanowire cavity with a diameter of 212 nm on the Ag film in the two- and three-dimensional simulation.
fig. S12. Spatial, momentum, and frequency space images of a nanowire spaser.

REFERENCES AND NOTES

1. T. H. Maiman, Stimulated optical radiation in ruby. *Nature* **187**, 493–494 (1960).
2. W. Srituravanich, N. Fang, C. Sun, Q. Luo, X. Zhang, Plasmonic nanolithography. *Nano Lett.* **4**, 1085–1088 (2004).
3. Z.-W. Liu, Q.-H. Wei, X. Zhang, Surface plasmon interference nanolithography. *Nano Lett.* **5**, 957–961 (2005).
4. L. Wang, S. M. Uppuluri, E. X. Jin, X. F. Xu, Nanolithography using high transmission nanoscale bowtie apertures. *Nano Lett.* **6**, 361–364 (2006).
5. W. A. Challener, C. Peng, A. V. Itagi, D. Karns, W. Peng, Y. Peng, X. M. Yang, X. Zhu, N. J. Gokemeijer, Y.-T. Hsia, G. Ju, R. E. Rottmayer, M. A. Seigler, E. C. Gage, Heat-assisted magnetic recording by a near-field transducer with efficient optical energy transfer. *Nat. Photonics* **3**, 220–224 (2009).
6. B. C. Stipe, T. C. Strand, C. C. Poon, H. Balamane, T. D. Boone, J. A. Katine, J.-L. Li, V. Rawat, H. Nemoto, A. Hirotsune, O. Hellwig, R. Ruiz, E. Dobisz, D. S. Kercher, N. Robertson, T. R. Albrecht, B. D. Terris, Magnetic recording at 1.5 Pb m^{-2} using an integrated plasmonic antenna. *Nat. Photonics* **4**, 484–488 (2010).
7. J. B. Pendry, Negative refraction makes a perfect lens. *Phys. Rev. Lett.* **85**, 3966–3969 (2000).
8. N. Fang, H. Lee, C. Sun, X. Zhang, Sub–diffraction-limited optical imaging with a silver superlens. *Science* **308**, 534–537 (2005).
9. A. Poddubny, I. Iorsh, P. Belov, Y. Kivshar, Hyperbolic metamaterials. *Nat. Photonics* **7**, 958–967 (2013).
10. D. J. Bergman, M. I. Stockman, Surface plasmon amplification by stimulated emission of radiation: Quantum generation of coherent surface plasmons in nanosystems. *Phys. Rev. Lett.* **90**, 027402 (2003).
11. S. I. Bozhevolnyi, V. S. Volkov, E. Devaux, J.-Y. Laluet, T. W. Ebbesen, Channel plasmon subwavelength waveguide components including interferometers and ring resonators. *Nature* **440**, 508–511 (2006).
12. J. A. Dionne, K. Diest, L. A. Sweatlock, H. A. Atwater, PlasMOStor: A metal-oxide-Si field effect plasmonic modulator. *Nano Lett.* **9**, 897–902 (2009).
13. R.-M. Ma, X. B. Yin, R. F. Oulton, V. J. Sorger, X. Zhang, Multiplexed and electrically modulated plasmon laser circuit. *Nano Lett.* **12**, 5396–5402 (2012).
14. K. C. Y. Huang, M.-K. Seo, T. Sarmiento, Y. Huo, J. S. Harris, M. L. Brongersma, Electrically driven subwavelength optical nanocircuits. *Nat. Photonics* **8**, 244–249 (2014).
15. B. Liedberg, C. Nylander, I. Lundstrom, Surface-plasmon resonance for gas-detection and biosensing. *Sens. Actuators* **4**, 299–304 (1983).
16. J. N. Anker, W. Paige Hall, O. Lyandres, N. C. Shah, J. Zhao, R. P. Van Duyne, Biosensing with plasmonic nanosensors. *Nat. Mater.* **7**, 442–453 (2008).
17. R.-M. Ma, S. Ota, Y. M. Li, S. Yang, X. Zhang, Explosives detection in a lasing plasmon nanocavity. *Nat. Nanotechnol.* **9**, 600–604 (2014).
18. M. I. Stockman, Nanoplasmonic sensing and detection. *Science* **348**, 287–288 (2015).
19. X.-Y. Wang, Y.-L. Wang, S. Wang, B. Li, X.-W. Zhang, L. Dai, R.-M. Ma, Lasing enhanced surface plasmon resonance sensing. *Nanophotonics* **5**, 52–58 (2016).
20. M. T. Hill, M. Marell, E. S. P. Leong, B. Smalbrugge, Y. Zhu, M. Sun, P. J. van Veldhoven, E. Jan Geluk, F. Karouta, Y.-S. Oei, R. Nötzel, C.-Z. Ning, M. K. Smit, Lasing in metal-insulator-metal sub-wavelength plasmonic waveguides. *Opt. Express* **17**, 11107–11112 (2009).
21. M. A. Noginov, G. Zhu, A. M. Belgrave, R. Bakker, V. M. Shalaev, E. E. Narimanov, S. Stout, E. Herz, T. Suteewong, U. Wiesner, Demonstration of a spaser-based nanolaser. *Nature* **460**, 1110–1112 (2009).
22. R. F. Oulton, V. J. Sorger, T. Zentgraf, R.-M. Ma, C. Gladden, L. Dai, G. Bartal, X. Zhang, Plasmon lasers at deep subwavelength scale. *Nature* **461**, 629–632 (2009).
23. R.-M. Ma, R. F. Oulton, V. J. Sorger, G. Bartal, X. Zhang, Room-temperature sub-diffraction-limited plasmon laser by total internal reflection. *Nat. Mater.* **10**, 110–113 (2011).
24. A. M. Lakhani, M.-k. Kim, E. K. Lau, M. C. Wu, Plasmonic crystal defect nanolaser. *Opt. Express* **19**, 18237–18245 (2011).
25. M. Khajavikhan, A. Simic, M. Katz, J. H. Lee, B. Slutsky, A. Mizrahi, V. Lomakin, Y. Fainman, Thresholdless nanoscale coaxial lasers. *Nature* **482**, 204–207 (2012).
26. Y.-J. Lu, J. Kim, H.-Y. Chen, C. Wu, N. Dabidian, C. E. Sanders, C.-Y. Wang, M.-Y. Lu, B.-H. Li, X. Qiu, W.-H. Chang, L.-J. Chen, G. Shvets, C.-K. Shih, S. Gwo, Plasmonic nanolaser using epitaxially grown silver film. *Science* **337**, 450–453 (2012).
27. W. Zhou, M. Dridi, J. Yong Suh, C. Hoon Kim, D. T. Co, M. R. Wasielewski, G. C. Schatz, T. W. Odom, Lasing action in strongly coupled plasmonic nanocavity arrays. *Nat. Nanotechnol.* **8**, 506–511 (2013).
28. F. van Beijnum, P. J. van Veldhoven, E. J. Geluk, M. J. A. de Dood, G. W. 't Hooft, M. P. van Exter, Surface plasmon lasing observed in metal hole arrays. *Phys. Rev. Lett.* **110**, 206802 (2013).
29. X. G. Meng, A. V. Kildishev, K. Fujita, K. Tanaka, V. M. Shalaev, Wavelength-tunable spasing in the visible. *Nano Lett.* **13**, 4106–4112 (2013).
30. Q. Zhang, G. Li, X. Liu, F. Qian, Y. Li, T. Chien Sum, C. M. Lieber, Q. Xiong, A room temperature low-threshold ultraviolet plasmonic nanolaser. *Nat. Commun.* **5**, 4953 (2014).
31. Y.-J. Lu, C.-Y. Wang, J. Kim, H.-Y. Chen, M.-Y. Lu, Y.-C. Chen, W.-H. Chang, L.-J. Chen, M. I. Stockman, C.-K. Shih, S. Gwo, All-color plasmonic nanolasers with ultralow thresholds: Autotuning mechanism for single-mode lasing. *Nano Lett.* **14**, 4381–4388 (2014).
32. C. Zhang, Y. Lu, Y. Ni, M. Li, L. Mao, C. Liu, D. Zhang, H. Ming, P. Wang, Plasmonic lasing of nanocavity embedding in metallic nanoantenna array. *Nano Lett.* **15**, 1382–1387 (2015).
33. M. C. Gather, A rocky road to plasmonic lasers. *Nat. Photonics* **6**, 708–708 (2012).
34. F. F. Lu, T. Li, J. Xu, Z. D. Xie, L. Li, S. N. Zhu, Y. Y. Zhu, Surface plasmon polariton enhanced by optical parametric amplification in nonlinear hybrid waveguide. *Opt. Express* **19**, 2858–2865 (2011).
35. F. M. Pigozzo, D. Modotto, S. Wabnitz, Second harmonic generation by modal phase matching involving optical and plasmonic modes. *Opt. Lett.* **37**, 2244–2246 (2012).
36. C. Shi, S. Soltani, A. M. Armani, Gold nanorod plasmonic upconversion microlaser. *Nano Lett.* **13**, 5827–5831 (2013).
37. J. H. Zhang, E. Cassan, X. L. Zhang, Efficient second harmonic generation from mid-infrared to near-infrared regions in silicon-organic hybrid plasmonic waveguides with small fabrication-error sensitivity and a large bandwidth. *Opt. Lett.* **38**, 2089–2091 (2013).
38. A. Drezet, A. Hohenau, D. Koller, A. Stepanov, H. Ditlbacher, B. Steinberger, F. R. Aussenegg, A. Leitner, J. R. Krenn, Leakage radiation microscopy of surface plasmon polaritons. *Mater. Sci. Eng. B* **149**, 220–229 (2008).
39. A. Hohenau, J. R. Krenn, A. Drezet, O. Mollet, S. Huant, C. Genet, B. Stein, T. W. Ebbesen, Surface plasmon leakage radiation microscopy at the diffraction limit. *Opt. Express* **19**, 25749–25762 (2011).
40. J. Laverdant, S. A. Guebrou, F. Bessueille, C. Symonds, J. Bellessa, Leakage interferences applied to surface plasmon analysis. *J. Opt. Soc. Am. A Opt. Image Sci. Vis.* **31**, 1067–1073 (2014).
41. C. Liu, P. Wu, T. Sun, L. Dai, Y. Ye, R. Ma, G. Qin, Synthesis of high quality *n*-type CdSe nanobelts and their applications in nanodevices. *J. Phys. Chem. C* **113**, 14478–14481 (2009).

Acknowledgments

Funding: This work was supported by the National Natural Science Foundation of China (nos. 11574012, 61521004, 61125402, 51172004, and 11474007), the Youth 1000 Talent Plan Fund, the National Basic Research Program of China (nos. 2013CB921901 and 2012CB932703), and the Ministry of Education of China (no. 201421). **Author contributions:** R.-M.M. conceived and provided guidance to the work. H.-Z.C., J.-Q.H., S.W., and B.L. carried out the experiments. H.-Z.C. and X.-Y.W. conducted theoretical simulations. Y.-L.W. and L.D. synthesized CdSe nanowires. All authors discussed the results. R.-M.M. and H.-Z.C. wrote the manuscript. **Competing interests:** The authors declare that they have no competing interests. **Data and materials availability:** All data needed to evaluate the conclusions in the paper are present in the paper and/or the Supplementary Materials. Additional data related to this paper may be requested from the authors.

Submitted 19 August 2016
Accepted 16 February 2017
Published 14 April 2017
10.1126/sciadv.1601962

Citation: H.-Z. Chen, J.-Q. Hu, S. Wang, B. Li, X.-Y. Wang, Y.-L. Wang, L. Dai, R.-M. Ma, Imaging the dark emission of spasers. *Sci. Adv.* **3**, e1601962 (2017).

ScienceAdvances

Imaging the dark emission of spasers

Hua-Zhou ChenJia-Qi HuSuo WangBo LiXing-Yuan WangYi-Lun WangLun DaiRen-Min Ma

Sci. Adv., 3 (4), e1601962. • DOI: 10.1126/sciadv.1601962

Science Advances (ISSN 2375-2548) is published by the American Association for the Advancement of Science. 1200 New York Avenue NW, Washington, DC 20005. The title *Science Advances* is a registered trademark of AAAS.